

CNN-based Surface Temperature Forecasts with Ensemble Numerical Weather Prediction over Medium-range Forecast Periods

Takuya Inoue, Takuya Kawabata

Meteorological Research Institute, Tsukuba, Ibaraki, Japan

Corresponding author: Takuya Inoue, inoue@mri-jma.go.jp

This Work has been submitted to Monthly Weather Review. Copyright in this Work may be transferred without further notice.

ABSTRACT

In this study, a method that integrates convolutional neural networks (CNNs) with ensemble numerical weather prediction (NWP) models is proposed. This method enables surface temperature forecasting with lead times beyond the short-range, extending up to five days. Due to limited computational resources, operational medium-range temperature forecasts typically rely on low-resolution NWP models, which are prone to systematic and random errors. To resolve these limitations, the proposed method applies CNN-based post-processing (bias correction and spatial super-resolution) to an ensemble NWP system. First, the post-processing is applied to each ensemble member to reduce systematic errors and reconstruct high-resolution temperature fields from low-resolution model outputs. This approach reduces the systematic and random errors in NWP model outputs and outperforms operational post-processing. Second, the CNN is applied to all ensemble members to construct a new ensemble forecasting system, in which deterministic forecast accuracy, probabilistic reliability, and representation of ensemble spread are improved compared with those of the original system. We demonstrate that this CNN-based post-processing is fundamentally different from the artificial error reduction caused by smoothing inherent in ensemble averaging because the post-processing reduces forecast errors without degrading the forecast information. These results indicate that the proposed method provides a practical and scalable solution for improving medium-range temperature forecasts and is particularly valuable for use in operational centers with limited computational resources.

SIGNIFICANCE STATEMENT

Reliable temperature forecasts lasting more than five days are vital for planning and public safety; however, current forecasting methods rely on low-resolution numerical weather prediction models that frequently misestimate temperatures. We developed a new method that employs artificial intelligence to correct each member of a set of forecasts (an “ensemble”), thereby reducing both systematic and random errors. This method provides more accurate, reliable, and detailed ensemble forecasts than the model’s original output while requiring less computing power. This method can help communities better prepare for temperature-related risks by making accurate forecasts accessible to operational centers with limited resources.

1. Introduction

Surface temperature is an important meteorological variable that influences sectors such as agriculture, transportation, tourism, energy demand, and public health (Frisvold and

Murugesan 2013; Xia et al. 2013; Wang et al. 2023; Chen et al. 2024; Yin et al. 2024). Decision-making in these sectors largely relies on the temperature forecasts of numerical weather prediction (NWP) models. Although improvements in model physics, data assimilation, and computational resources have enhanced the predictive accuracy of NWP models (Kawabata et al. 2007; 2011, Bauer et al. 2015, Ikuta et al. 2021), the model outputs are prone to systematic and random errors (Stensrud 2007). Systematic errors arise from factors such as inherent model imperfections and limited horizontal resolution of complex topography, whereas random errors are primarily sourced from uncertainties in initial conditions (Lorenz 1969; Palmer 2001; Skamarock 2004).

In most NWP models, a trade-off exists between horizontal resolution and forecast lead time. High-resolution models often shorten the forecast range to prevent the overload of limited computational resources, whereas low-resolution models allow longer forecast lead times. Both systematic and random errors tend to accumulate with decreasing resolution and increasing forecast lead time. Various post-processing techniques have been employed to address these issues. Traditional methods such as model output statistics (Glahn and Lowry 1972) and Kalman filtering (KF) (Homleid 1995; Anadranistakis et al. 2004) have been widely used because they effectively reduce systematic errors in NWP forecasts.

Deep learning has recently emerged as a promising post-processing tool for NWP forecasts, particularly for bias correction and downscaling. In particular, convolutional neural networks (CNNs), which extract hierarchical features using combined convolutional and pooling layers, are widely used in image recognition (Krizhevsky et al. 2012; Simonyan and Zisserman 2015) and NWP fields to capture spatial error structures. Sayeed et al. (2023) employed CNNs for correcting biases in multiple meteorological variables derived from the Weather Research and Forecasting (WRF) model. Kudo (2022) employed an encoder–decoder CNN architecture to improve the surface temperature forecasts of operational NWP models, successfully resolving the errors in frontal position prediction. Inoue et al. (2024) integrated CNN-based post-processing with KF to improve both gridded and point-based surface temperature predictions. These studies indicate that CNNs can effectively reduce systematic errors and enhance spatial resolution of NWP forecasts.

Forecast uncertainty can also be quantified using ensemble prediction methods (Leith 1974; Toth and Kalnay 1997, Wu et al. 2025), which represent uncertainties in initial and boundary conditions as well as model physics. Ensemble averaging reduces random errors, as demonstrated in the global ensemble forecast dataset produced under the international

program The Observing system Research and Predictability Experiment (THORPEX), namely THORPEX Interactive Grand Global Ensemble (TIGGE). However, ensemble averaging inherently smooths spatial structures (Swinbank et al. 2016), thereby degrading the representation of fine-scale features and extremes in predictions. Moreover, systematic errors remain even after ensemble averaging, which must be addressed by employing bias-correction techniques (Wang et al. 2018).

The Japan Meteorological Agency (JMA) operates the Global Ensemble Prediction System (GEPS; Japan Meteorological Agency 2023), a global-scale ensemble forecast system that supports medium-range weather prediction. The GEPS comprises 51 ensemble members generated by perturbing the initial conditions of a single NWP model to replicate forecast uncertainty. However, due to its low horizontal resolution, the GEPS cannot capture fine-scale temperature variabilities, particularly in topographically complex regions. Therefore, the GEPS accuracy must be enhanced by employing post-processing techniques such as bias correction and statistical downscaling.

CNNs have been recently integrated with ensemble forecasting. For instance, Sha et al. (2022) and Hess and Boers (2022) applied CNNs to ensemble NWP outputs for precipitation forecasting. However, these approaches typically operate on ensemble means or selected summary statistics, which do not explicitly exploit the full variability among individual ensemble members. Consequently, the role of CNN correction applied at the ensemble-member level and its interaction with ensemble averaging remain unclear. In particular, the following knowledge gaps are yet to be well addressed: (i) which ensemble members should be used as training data for CNNs? (ii) how CNNs improve the deterministic and probabilistic prediction skills? (iii) what is the relationship between ensemble averaging and smoothing effects?

For addressing these gaps, a unified post-processing framework that integrates CNN-based bias correction and super-resolution with ensemble forecasting is employed herein for medium-range surface temperature prediction. Using this approach, we aim to answer the following scientific questions:

Q1. How effectively can a CNN-based post-processing framework, applied to individual ensemble members, reduce systematic and random errors in NWP forecasts?

Q2. How does the selection of an ensemble member for training influence the performance of CNN-based post-processing?

Q3. How does CNN-based post-processing improve the reliability, spread–skill balance, and the relationship between ensemble averaging and smoothing effects?

The remainder of this paper is organized as follows. Section 2 describes the datasets and preprocessing procedures. The proposed CNN architecture and associated verification metrics are introduced in Section 3. Section 4 outlines the experimental setup, and Section 5 presents the results and their comparison with the results of other models and case studies. Section 6 discusses the implications and limitations of the proposed method, and Section 7 concludes the paper with key findings and future directions.

2. Data

a. Deterministic NWP Models

Herein, two deterministic NWP models operated by the JMA are employed as reference for comparison: the global spectral model (GSM; Japan Meteorological Agency 2023) and the mesoscale model (MSM; Japan Meteorological Agency 2023). The GSM is a global hydrostatic model with a horizontal resolution of approximately 20 km in this study. Forecasts are generated with lead times of 216 h from 0000 and 1200 UTC and 132 h from 0600 and 1800 UTC, and output data are provided every 6 h for each forecast. Herein, GSM forecasts with a lead time of 132 h from 0000 and 1200 UTC are used to ensure consistency with the GEPS dataset.

The MSM with a horizontal resolution of 5 km employing the nonhydrostatic regional NWP model provides detailed forecasts. This model is operated eight times per day and provides forecasts with lead times of up to 51 h ahead. Forecasts initialized at 0000 and 1200 UTC are used to maintain temporal consistency with the GEPS and GSM datasets. Owing to its high spatial resolution, the MSM can capture small-scale features such as local temperature variations and precipitation associated with complex terrain. Therefore, the performance of the proposed method is evaluated against MSM output.

Herein, medium-range forecasts are referred to as predictions extending from beyond 3 days up to 10 days (72–240 h) ahead, following standard meteorological convention (World Meteorological Organization 2023). Accordingly, the GSM is classified as a medium-range NWP model, whereas the MSM is primarily used as a short-range reference for validation.

b. Ensemble NWP Model

The GEPS provides global-scale forecasts based on a low-resolution ensemble system; it was introduced into the operational system of the JMA on 17 January 2017. Initially, the GEPS comprised 27 ensemble members with a horizontal resolution of 40 km, which was expanded to 51 members on 30 March 2021. GEPS forecasts are initialized four times per day (0000, 0600, 1200, and 1800 UTC). The forecast range depends on the initialization time and day of the week, varying from 132 h for the 0600 and 1800 UTC runs to 34 days for the 1200 UTC runs on Tuesdays and Wednesdays. To ensure consistency with the deterministic models described previously, GEPS forecasts initialized at 0000 and 1200 UTC with lead times up to 132 h are used. The ensemble forecasts involve one control forecast (CF), which generally employs the same physical parameterization schemes as the GSM but at a different lower resolution, and 50 perturbed forecasts (PFs). The perturbations are generated by combining singular vectors (Buizza and Palmer 1995) and the local ensemble transform KF (Hunt et al. 2007). Although the operational resolution of GEPS was upgraded to 27 km on 15 March 2022, 40-km resolution data are employed herein to ensure consistent data usage between training and inference across models.

c. Post-Processed Baseline

The JMA applies a KF-based post-processing system for the correction of systematic errors in NWP temperature forecasts (Sannohe 2018). The KF system first predicts the 1.5-m air temperature at surface observation stations in Japan via the statistical regression of data derived from nearby NWP grid points. Although the World Meteorological Organization (2024) recommends placing air-temperature sensors at a screen height between 1.25 and 2 m above ground level, JMA adopts 1.5 m as its operational standard. The KF sequentially updates the regression coefficients based on real-time observations. The advantage of this sequential updating is that it allows the correction to follow time-varying NWP biases (including seasonal variations and model upgrades), adapt to changes in station environments (e.g., relocations), and accommodate newly established stations without requiring a long-term observational dataset. The resulting point-based forecasts are interpolated onto spatial regular grids via weighted averaging that accounts for topography and distance (Kuroki 2017), yielding bias-corrected temperature forecasts at a horizontal resolution of 5 km.

In addition to employing the GSM–KF system as the baseline, the same KF-based framework is applied to high-resolution MSM forecasts and used as an additional baseline method. Although the GSM–KF and MSM–KF systems have short forecast ranges (84 and 51

h, respectively), they provide effective bias correction and are strong baseline methods for evaluating post-processing methods.

d. Ground-truth Surface Temperature

The 1.5-m air temperatures derived from the operational weather distribution products of the JMA are used as ground-truth data (Wakayama et al. 2020). These products provide hourly gridded data at a resolution of 1 km for surface temperature, weather category, and sunshine duration across Japan. Surface temperatures are estimated from the combined observations at more than 900 stations and the gridded climatological normal. This normal is derived using a multiple linear regression model that relates the 30-year average temperatures at each observatory, topographic information, and various urban factors. This model enables reliable temperature estimations even in locations lacking direct observations. The accuracy of this dataset is evaluated via cross-validation against actual observations from January 2013 to May 2015. For each grid cell containing an observation station, the estimated temperature is compared with the observed value at that station using a leave-one-out approach, in which the target station is excluded from estimations. The bias and root mean square error (RMSE) are approximated as 0.01 and 1.19 K, respectively, indicating the high accuracy of the dataset (Japan Meteorological Agency 2016). These values represent the nationwide average across Japan, including mountainous regions, where both interpolation errors and extreme temperature variability are relatively larger compared with those over plains. Within the common temperature range ($-5\text{ }^{\circ}\text{C}$ - $25\text{ }^{\circ}\text{C}$), the RMSE is approximately 1 K and is below 1 K over the plains considered in case studies.

Herein, the estimated temperatures are gridded onto a 5-km mesh to ensure consistency with the 5-km resolution of the GSM-KF system. These 5-km-averaged estimated surface temperatures (ESTs) are treated as the target (ground truth) for evaluating gridded temperature predictions.

e. Summary of Datasets

Several datasets provided by the JMA are used as inputs and references for evaluating the proposed method. The GEPS is the main input dataset for CNN-based bias correction and super-resolution. The GSM provides high-resolution deterministic forecasts based on generally the same physical parameterization schemes as those of the GEPS. For comparative evaluations, the MSM is adopted as a high-resolution dataset and the GSM-

KF and MSM–KF systems are adopted as high-resolution post-processed datasets. The 5-km gridded EST dataset is used as the ground truth for both training and evaluation. This dataset comprises periods extending from 0000 UTC 17 January 2017 to 1200 UTC 31 December 2022 at 12-h intervals; it is divided into training, validation, and test periods, as summarized in Table 1.

Dataset Category	Time Period	Data
Training	17 January 2017–31 December 2020	GEPS (40 km), GSM (20 km), and EST (5 km)
Validation	1 January 2021–31 December 2021	GEPS, GSM, and EST
Test	1 January 2022–31 December 2022	GEPS, GSM, EST, MSM (5 km), GSM–KF (5 km), and MSM–KF (5 km)

Table 1. Categories and time periods of datasets used for training, validating, and testing the CNN model.

3. Methods

a. CNN Model

The CNN-based post-processing framework mitigates the errors introduced by low grid resolutions, terrain-induced biases, and systematic deviations in NWP forecasts.

Figure 1 and Table 2 summarize the CNN architecture and hyperparameters, respectively. The proposed model is based on the encoder–decoder CNN architectures developed by Kudo (2022) and Inoue et al. (2024), which capture spatial patterns in meteorological data derived from NWP models and accurately reconstruct temperature fields. The encoder–decoder structure effectively learns the spatial correlations among meteorological variables, thereby facilitating the refinement of local temperature fields. The CNN architecture comprises convolutional layers, pooling layers, and fully connected layers. The rectified linear unit (ReLU) activation functions (Nair and Hinton 2010) are added in the intermediate layers and a sigmoid activation function is added in the output layer to constrain the predictions within a realistic range. Batch normalization is applied to stabilize training and increase convergence.

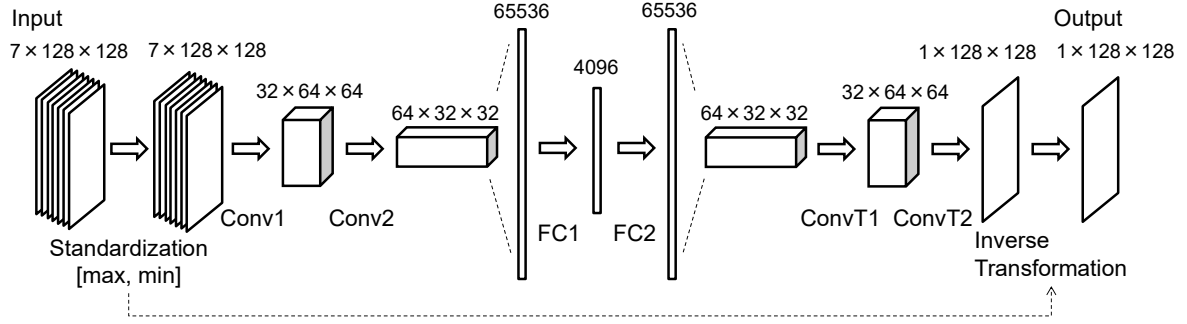


Fig. 1. Schematic of the CNN (reprinted from our previous work: Fig. 1. in Inoue et al. 2024). Conv1, Conv2, and other operational units are detailed in Table 2.

Unit	Function	Parameters
Conv1	Conv2d	kernel_size = 5, stride = 1, padding = 2, number of channels: 7 to 32
	MaxPool2d	kernel_size = 2, stride = 2
	BatchNorm2d	number of channels: 32
	ReLU	
Conv2	Conv2d	kernel_size = 5, stride = 1, padding = 2, number of channels: 32 to 64
	MaxPool2d	kernel_size = 2, stride = 2
	BatchNorm2d	number of channels: 64
	ReLU	
FC1	Linear	number of units: 65536 to 4096
	BatchNorm1d	number of units: 4096
	ReLU	
FC2	Linear	number of units: 4096 to 65536
	BatchNorm1d	number of units: 65536
	ReLU	

ConvT1	ConvTranspose2d	kernel_size = 2, stride = 2, padding = 0, number of channels: 64 to 32
	BatchNorm2d	number of channels: 32
	ReLU	
ConvT2	ConvTranspose2d	kernel_size = 2, stride = 2, padding = 0, number of channels: 32 to 1
	BatchNorm2d	number of channels: 1
	Sigmoid	

Table 2. Functions and parameters used in the CNN shown in Fig. 1 (based on Table 1 in the paper by Inoue et al. 2024).

The CNN model is trained using seven meteorological variables obtained from NWP outputs: surface temperature, temperatures at 975, 925, and 850 hPa, mean sea-level pressure, and the zonal (U) and meridional (V) components of the surface wind. These variables are selected because they influence the surface temperature via thermodynamic and dynamical processes. Additional inputs such as time-of-day information and static predictors such as topographic information are not explicitly included as CNN inputs because surface temperatures exhibit strong diurnal variability and elevation-related effects manifest as systematic errors. Therefore, these factors are assumed to be learned implicitly from temperature fields, similar to those in previous studies (Kudo 2022; Inoue et al. 2024). All input variables are normalized to the [0, 1] range to improve training stability and ensure consistent scaling across different meteorological parameters. Following Kudo (2022)’s approach, the following simple min–max normalization is used for standardization:

$$\phi' = \frac{\phi - \phi_{\min}}{\phi_{\max} - \phi_{\min}}, \quad (1)$$

where ϕ and ϕ' denote the original and normalized variables, respectively, and ϕ_{\max} and ϕ_{\min} denote the spatial maximum and minimum values of NWP outputs, respectively, at each target time. This normalization method yields a more uniform distribution of normalized variables within the [0, 1] range compared with that based on maximum and minimum values derived during model training. To account for extreme temperatures that fall outside the

range predicted by NWP models, temperatures at the surface and 975, 925, and 850 hPa are standardized using +3 K and -3 K as the maximum and minimum values, respectively. The same range is applied for the inverse transformation of the CNN outputs and for normalizing the EST dataset used as the ground truth. Although topographic information is not explicitly used as the input to the CNN, a land-sea mask is applied so that only land grid points are used to compute the loss function. Thus, the CNN outputs are evaluated exclusively over land areas.

Experiments are conducted over central Japan (Fig. 2), which is chosen for its high population density, diverse topography, and relatively large seasonal variability in surface temperature. This region encompasses both plains and mountainous areas, making it an ideal testbed for evaluating the effectiveness of CNN-based post-processing. This region is particularly ideal for evaluating whether CNN correction can mitigate terrain-induced temperature biases and improve the spatial detail of forecasts.

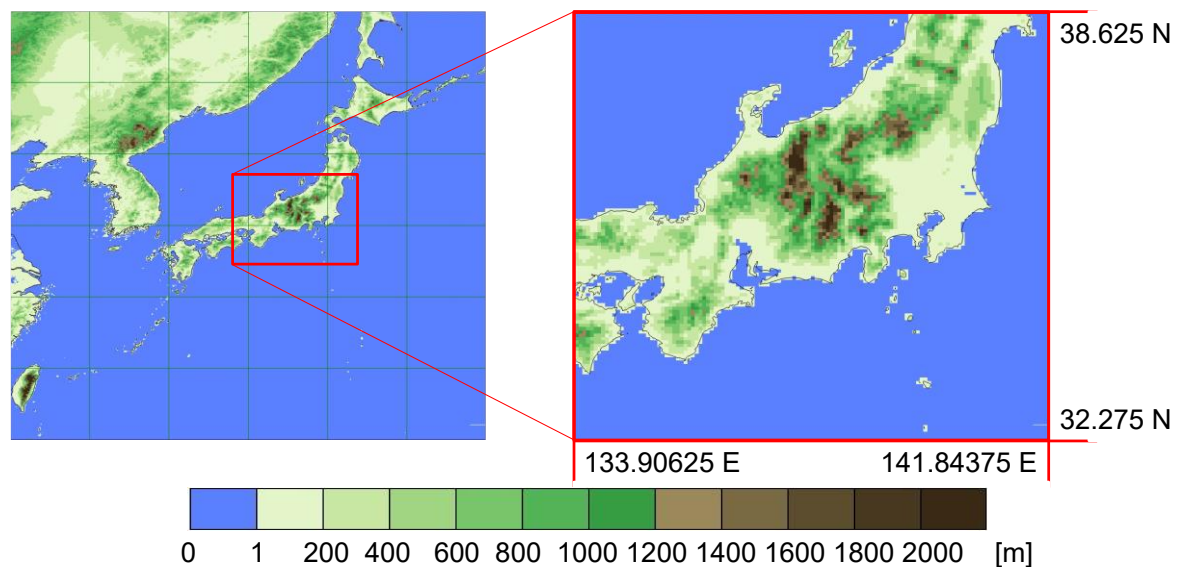


Fig. 2. Islands of Japan located in the Far East (left) and the target domain (right). The color scale indicates elevation. Only the land area is targeted herein.

b. CNN-based Error Correction and Super-resolution

During the training phase, the CNN learns to correct systematic errors and enhance the spatial resolution by mapping the low-resolution NWP outputs to high-resolution gridded observational data. The explanatory variables are the NWP data at horizontal resolutions of 40 km (GEPS) or 20 km (GSM), and the target variable is the 5-km resolution EST. After learning this mapping, the CNN performs bias correction and statistical downscaling by

reconstructing high-resolution spatial structures from low-resolution forecasts. In this context, the CNN functions as a super-resolution model. In addition, it captures various sources of forecast errors, such as biases introduced by the low resolution of the terrain. It minimizes these errors via training and establishing a data-driven relationship, enabling the correction of both biases to enhance the horizontal resolution.

During inference, the trained CNN estimates surface temperatures from the NWP outputs; it thus improves forecast accuracy and enhances the spatial detail. Hereafter, the CNN-corrected forecasts are appended with “-CNN” as follows: CF-CNN for the CNN-corrected CF, GSM-CNN for the CNN-corrected GSM, and GEPS-CNN for the ensemble forecast of each individually CNN-corrected GEPS member.

In the experiments, the CNN is trained using the CF; the trained network is then applied to each PF. As the CF and PFs share identical model configurations, except for their initial conditions, the error characteristics learned from the CF are expected to be statistically transferable to the PFs. This expectation is confirmed in Section 4b (Exp_Mem), and the corresponding results are discussed in Section 5b. This design enables consistent bias correction across all ensemble members while keeping computational costs reasonable.

c. Ensemble Averaging

Each ensemble member represents uncertainties arising from initial conditions, boundary conditions, and physical parameterization schemes. Ensemble averaging, which reduces random errors in individual forecasts (Leith 1974), is defined as follows:

$$\bar{f}(t) = \frac{1}{M} \sum_{i=1}^M f_i(t), \quad (2)$$

where $\bar{f}(t)$ represents the ensemble mean at time t , M is the total number of ensemble members, and $f_i(t)$ denotes the forecast of the i -th ensemble member.

The ensemble means are appended with “-EM.” Specifically, GEPS-EM represents the ensemble mean of the GEPS members and CNN-EM denotes the mean of a CNN-corrected GEPS member (GEPS-CNN).

d. Integration of CNN-based Post-processing and Ensemble Model

To overcome the limitations of low-resolution ensemble forecasts, CNN-based bias correction and super-resolution are integrated into an operational ensemble prediction system.

Then, CNN-based post-processing is applied to the GEPS comprising one CF and 50 PFs (Fig. 3). During inference, the trained CNN is applied separately to the CF and all 50 PFs. This approach reduces systematic errors and enhances the effective horizontal resolution, yielding a 51-member CNN-corrected ensemble (GEPS–CNN). Standard ensemble statistics, such as the ensemble mean and probabilistic verification scores, are then computed from the original GEPS and GEPS–CNN; this enables the assessment of how member-wise CNN correction affects deterministic skill, ensemble spread, and forecast reliability.

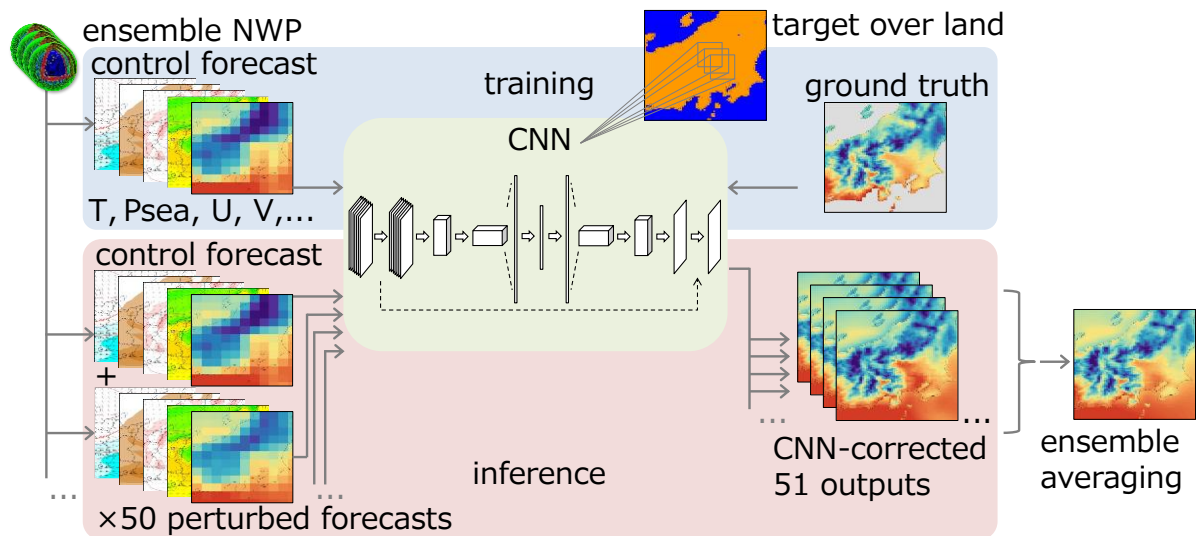


Fig. 3. Schematic of CNN-based post-processing applied to the GEPS. During training (upper panel), the CNN learns mapping parameters from the low-resolution fields of the CF (such as temperature, mean sea-level pressure, and winds) to high-resolution gridded analyses over land. During inference (lower panel), the trained CNN is applied to the CF and all 50 PFs to produce a 51-member CNN-corrected ensemble, from which ensemble statistics such as the ensemble mean are computed.

e. Verification Methods

To evaluate the effectiveness of the proposed method, the prediction accuracy of the surface temperature is assessed at each grid point within the target area (Fig. 2) from 1 January to 31 December 2022. GEPS forecasts and EST data are used as the input and ground-truth data, respectively. The GEPS and GSM forecasts with horizontal resolutions of 40 and 20 km, respectively, are interpolated to a 5-km grid using a bicubic function, and their forecasts are compared with the EST data. Forecasts are initialized at 0000 and 1200 UTC and validated at 12-h intervals.

The primary evaluation metric is the RMSE, which quantifies the overall magnitude of forecast errors (Wilks 2011):

$$\text{RMSE} = \sqrt{\frac{1}{N} \sum_{n=1}^N (F_n(\tau) - O_n(\tau))^2}, \quad (3)$$

where N represents the number of grid points and $F_n(\tau)$ and $O_n(\tau)$ denote the forecast and observed temperatures, respectively, at location n and forecast lead time τ . A lower RMSE indicates a higher forecast accuracy.

The second evaluation metric is the mean error (ME), which quantifies the average bias between the predicted and observed values:

$$\text{ME} = \frac{1}{N} \sum_{n=1}^N (F_n(\tau) - O_n(\tau)), \quad (4)$$

where N , $F_n(\tau)$, and $O_n(\tau)$ are defined in Eq. (2). An ME close to zero indicates minimal bias in forecasts, implying that the positive and negative errors largely cancel. In contrast, a non-zero ME indicates a systematic overestimation (positive ME) or underestimation (negative ME).

To further evaluate the ensemble forecast, the continuous ranked probability score (CRPS; Hersbach. H 2000) and ensemble spread are computed. The CRPS is a statistical metric widely used for probabilistic forecast evaluations and is calculated as follows:

$$\text{CRPS}(f_j(\tau), O(\tau)) = \frac{1}{M} \sum_{j=1}^M |f_j(\tau) - O(\tau)| - \frac{1}{2M(M-1)} \sum_{j=1}^M \sum_{\substack{k=1 \\ k \neq j}}^M |f_j(\tau) - f_k(\tau)|, \quad (5)$$

where $f_j(\tau)$ and $f_k(\tau)$ are the forecasts of the j and k -th ensemble members at forecast lead time τ , respectively, M is the total number of ensemble members, and $O(\tau)$ is the observed value. Low CRPSs indicate high probabilistic forecast skill. The CRPS is computed at each grid point and then averaged over all grid points to obtain a single score at each forecast lead time t .

The ensemble spread, representing the variability among ensemble members, is computed as the standard deviation across ensemble members:

$$S(t) = \sqrt{\frac{1}{M-1} \sum_{j=1}^M (f_j(t) - \bar{f}(t))^2}, \quad (6)$$

where $S(t)$ represents the ensemble spread at time t and $\bar{f}(t)$ is the ensemble mean defined by Eq. (1). The ensemble spread measures the dispersion among ensemble members and indicates whether the ensemble appropriately represents forecast uncertainty.

To assess ensemble reliability, rank histograms (Hamill 2001) are computed using all ensemble members at each forecast lead time. A flat rank histogram indicates a statistically reliable ensemble, whereas a U-shaped (underdispersive) or dome-shaped (overdispersive) distribution indicates an excessively narrow or excessively wide ensemble spread, respectively.

The spread–skill ratio (SSR) is also computed to quantify the consistency between ensemble spread and forecast error. It is the ratio of the ensemble spread (Eq. 6) to the RMSE (Eq. 2) of the ensemble-mean forecast. An SSR close to 1 indicates a well-calibrated ensemble, in which the spread is consistent with the actual forecast error variance, whereas values less than (greater than) 1 indicate underdispersion (overdispersion).

To further investigate the relationship between forecast skill, variance, and correlation, the forecast information (FI), noise error (NE), and anomaly correlation coefficient (ACC) are computed based Bonavita and Geer’s study (2025; hereafter BG25). The relationships among these quantities are represented geometrically using the triangle framework proposed by Feng et al. (2024; hereafter FTZP24) and BG25 (Fig. 4). In this framework, the sides correspond to the standard deviations of analysis anomaly (SDAV), the standard deviation of forecast anomaly (SDAF), and the standard deviation of error (STDE). The SDAF, which is the length of the forecast-anomaly vector, represents the forecast activity. The covariance between the forecast and observation anomalies is denoted by p , and the angle θ between the two anomaly vectors defines the ACC as follows.

$$\text{ACC} = \cos\theta = \frac{p}{\text{SDAF} \times \text{SDAV}}. \quad (7)$$

The FI and NE are derived from the projection of the forecast-anomaly vector onto the observed anomaly vector. The FI quantifies the useful (correlated) component of forecast variance, whereas the NE represents the uncorrelated (noise) component:

$$FI = \frac{p}{SDAF^2}, \quad NE = SDAF\sqrt{1 - ACC^2}. \quad (8)$$

The information error (IE), corresponding to the unexplained component of the observed anomaly variance, is given by

$$IE = |1 - FI| \times SDAV. \quad (9)$$

The FI, representing the fraction of the covariance p explained by the variance of observed anomalies, and NE together correspond to an orthogonal decomposition of the forecast variance into information and noise components (Fig. 4). A forecast system with high FI and low NE retains a large proportion of the observed variability and thus exhibits high predictive skills.

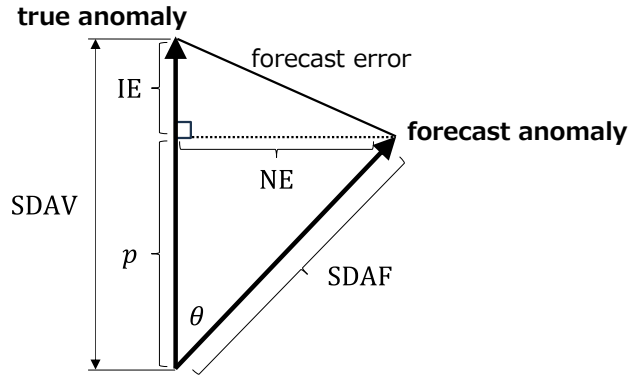


Fig. 4. Geometric representation of the relationships between true and forecast anomalies used in the definitions of FI, NE, and ACC (Feng et al. 2024; Bonavita and Geer 2025).

In addition to scalar verification metrics, quantile–quantile (Q–Q) plots are used to assess the consistency between the forecast and observed distributions. For each forecast field F and observation O , the quantiles $q_p(F)$ and $q_p(O)$ are computed for probability levels $p \in [0.01, 0.99]$ at an interval of 0.01. These forecast quantiles are plotted against the corresponding observed quantiles. This graphical approach is particularly useful for assessing how well the forecasts reproduce the spread and extremes, which are not fully captured by aggregated scores such as the CRPS.

4. Experiments

a. Exp_Det: Deterministic Model Correction

To evaluate the performance of CNN-based post-processing, a CNN is trained on the CF and applied to the same dataset during inference, yielding CF-CNN. The corrected forecasts in CF-CNN are compared with those in the baseline GSM-KF and MSM-KF systems at the same 5-km horizontal resolution. CF-CNN is also compared with the forecasts from the operational NWP models (GSM and MSM) used as inputs for the GSM-KF and MSM-KF systems. Note that the MSM has a native horizontal resolution of 5 km even before KF post-processing.

An additional CNN is trained using the GSM outputs and applied to the GSM dataset during inference, yielding GSM-CNN. By comparing GSM-CNN with CF-CNN, which employ the same physical parameterization schemes as the GSM but have different horizontal resolutions (40 km for CF vs. 20 km for GSM), the performance of CNN-based post-processing at different input resolutions can be evaluated.

Abbreviation	Description	Horizontal Resolution
CF	Control forecast of the GEPS	40 km
GSM	Global spectral model, which shares the same physical parameterization schemes as the GEPS	20 km
MSM	Mesoscale model (used as short-range reference)	5 km
GSM-KF	GSM corrected with a Kalman filter (used as post-process reference)	5 km
MSM-KF	MSM corrected with a Kalman filter (used as post-process reference)	5 km
CF-CNN	CF corrected with a CNN	5 km
GSM-CNN	GSM (different horizontal resolution from CF) corrected with a CNN	5 km

Table 3. Descriptions of the abbreviations used in Section 4a (Exp_Det)

b. Exp_Mem: Member-based Training Comparison

To determine whether training the CNN on the CF is the optimal approach, in experiment Exp_Mem, CNNs are trained using the CF, one PF (PF10; the 10th member is selected as a representative example), and the GEPS-EM.

Each trained model (CNN (CF), CNN (PF10), and CNN (EM)) is applied to both CF and PF (e.g., CF-CNN (PF10) and PF-CNN (PF10)), and their ensemble means are computed (CNN (CF)-EM, CNN (PF10)-EM, and CNN (EM)-EM). To ensure a consistent comparison, the same CNN architecture and training settings are used for all configurations.

Abbreviation	Description	Horizontal Resolution
PF10	The 10th GEPS perturbed forecast (PF)	40 km
GEPS-EM	Ensemble mean of the GEPS (CF and 50 PFs)	40 km
CF/PF-CNN (CF/PF10/GEPS-EM)	CF or PF corrected with the CNN trained using the CF, PF10, or GEPS-EM	5 km
CNN (CF/PF10/GEPS-EM)	GEPS (CF and 50 PF) corrected with the CNN trained using the CF, PF10, or GEPS-EM	5 km
CNN (CF/PF10/GEPS-EM)-EM	Ensemble mean of a CNN (CF/PF10/EM)	5 km

Table 4. Descriptions of the abbreviations used in Section 4b (Exp_Mem)

c. Exp_Ens: Ensemble Application

A CNN trained using the CF is applied to all 51 GEPS members, including one CF and 50 PFs. To compare the overall performance of the two ensemble forecasting systems before and after CNN correction, the ensemble mean of the original GEPS forecasts (EM) is compared with that of the CNN-corrected forecasts (CNN-EM). The ensemble-mean and member-wise results are examined with those from the deterministic GSM and MSM models,

baselines of the GSM–KF and MSM–KF systems, and the CNN-corrected GSM forecasts (GSM–CNN).

Abbreviation	Description	Horizontal Resolution
CF	GEPS control forecast	40 km
PF	GEPS perturbed forecast	40 km
EM	Ensemble mean of the CF and 50 PFs	40 km
GSM	Global spectral model	20 km
MSM	Mesoscale model	5 km
GSM–KF	GSM corrected with a Kalman filter	5 km
MSM–KF	MSM corrected with a Kalman filter	5 km
GSM–CNN	GSM corrected with a CNN	5 km
CF–CNN	CF corrected with a CNN	5 km
PF–CNN	PF corrected with a CNN	5 km
CNN–EM	Ensemble mean of the CF–CNN and 50 PF–CNNs	5 km

Table 5. Descriptions of the abbreviations used in Section 4c (Exp_Ens)

5. Results

a. Exp_Det: Deterministic Model Correction

Figure 5 shows the verification results of deterministic forecasts before and CNN after post-processing. Before post-processing, higher-resolution models exhibit smaller RMSEs (40 km CF > 20 km GSM > 5 km MSM). After post-processing, all forecasts evaluated at 5-km horizontal resolution show reduced RMSEs compared with their original systems. The lead-time-averaged RMSEs decrease by 0.76 and 0.99 K for the GSM–KF and GSM–CNN forecasts, respectively. The CF–CNN achieves a 1.2 K (46%) improvement relative to the

original CF. With KF-based correction, the lead-time-averaged absolute MEs are reduced by 0.07 K for the GSM–KF system relative to the GSM and by 0.21 K for the MSM–KF system relative to the MSM. However, as the absolute MEs of the GSM and MSM are originally larger than that of the CF up to a lead time of 72 h, the GSM–KF and MSM–KF systems remain comparable to the CF in terms of ME after correction. In contrast, CNN correction reduces the lead-time-averaged absolute ME by 0.18 K for the CF–CNN relative to the CF and 0.13 K for the GSM–CNN relative to the GSM; both MEs fall within ± 0.05 K.

These results indicate that CNN-based post-processing outperforms KF-based post-processing in reducing the ME and RMSE; however, no statistically significant difference is found between CF–CNN and GSM–CNN although the input forecasts have different original horizontal resolutions (40 km for the CF and 20 km for the GSM).

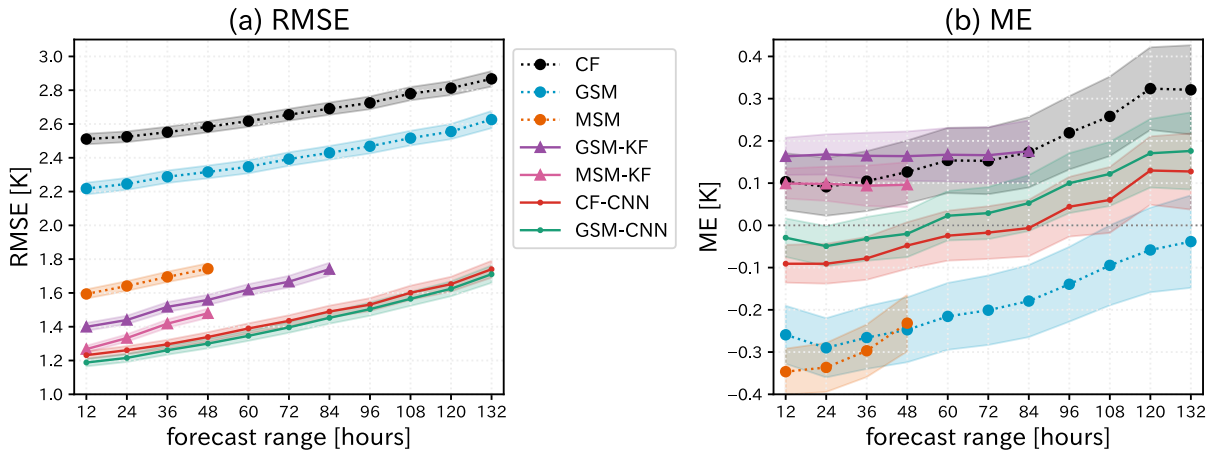


Fig. 5. (a) RMSEs and (b) MEs of the CF, GSM, MSM, GSM–KF, MSM–KF, CF–CNN, and GSM–CNN averaged over the 1 January to 31 December 2022 period. The shaded areas represent the 95% confidence intervals.

b. Exp_Mem: Member-based Training Comparison

The performances of ensemble forecasts when CNNs are trained using different ensemble members are examined. In this experiment, separate CNNs are trained using the CF, PF10, and the GEPS–EM (Fig. 6).

After CNN-based post-processing, the CF and PFs show substantial improvement and their lead-time-averaged RMSEs reduces by approximately 1.2 K. The RMSE difference between the CF and PFs slightly increases from 0.14 K (pre-CNN) to 0.20 K (post-CNN). This is possibly because the CNN primarily removes error components common to all ensemble members such as biases associated with model resolution, topographic information,

and physical parameterization schemes, whereas member-specific errors, which are relatively larger in the PFs due to initial-condition perturbations, remain even after post-processing. The RMSE curves of the CNN-corrected PFs trained using the CF, PF10, and GEPS-EM almost completely overlap, indicating their highly similar performances.

Figure 6b shows the SSR as an indicator of the overall ensemble reliability. All CNN-corrected ensembles show improved SSR compared with the original GEPS; however, no statistically significant differences are found among the three CNNs. This indicates that the CNN can be trained using any ensemble member; therefore, the CF is used as the training data in experiments.

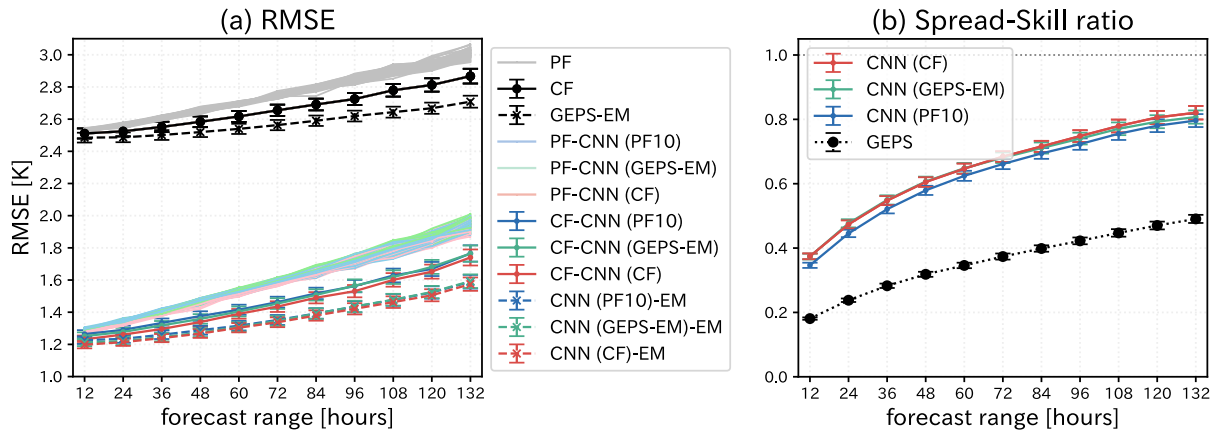


Fig. 6. (a) Average RMSEs and (b) SSRs of the models at different forecast lead times from 1 January to 31 December 2022. Error bars represent the 95% confidence intervals. Gray and pink, light blue, and light green shaded regions are the visual aggregations (thin lines) of 50 ensemble members (PF and PF-CNN (CF/PF10/GEPS-EM), respectively). The SSRs are calculated from all GEPS members and the ensembles corrected by each CNN.

c. *Exp_Ens: Ensemble Application*

In experiment *Exp_Ens*, the characteristics of ensemble forecasts before and after CNN-based post-processing are evaluated. Figure 7a shows the mean CRPSs for GEPS and GEPS-CNN, and Fig. 7b shows the corresponding rank histograms. The CNN considerably improves the CRPSs at all forecast lead times, indicating that the probability distributions of the CNN-corrected ensemble forecasts are closer to the observations. The SSR close to 1.0 (Fig. 6b) and the flatter rank histogram indicate that CNN-based post-processing mitigates the systematic underdispersion in the original GEPS ensemble. These results indicate that CNN-based post-processing improves the forecast accuracy and ensemble spread, enhancing deterministic forecast skill and the overall reliability of the ensemble forecasts.

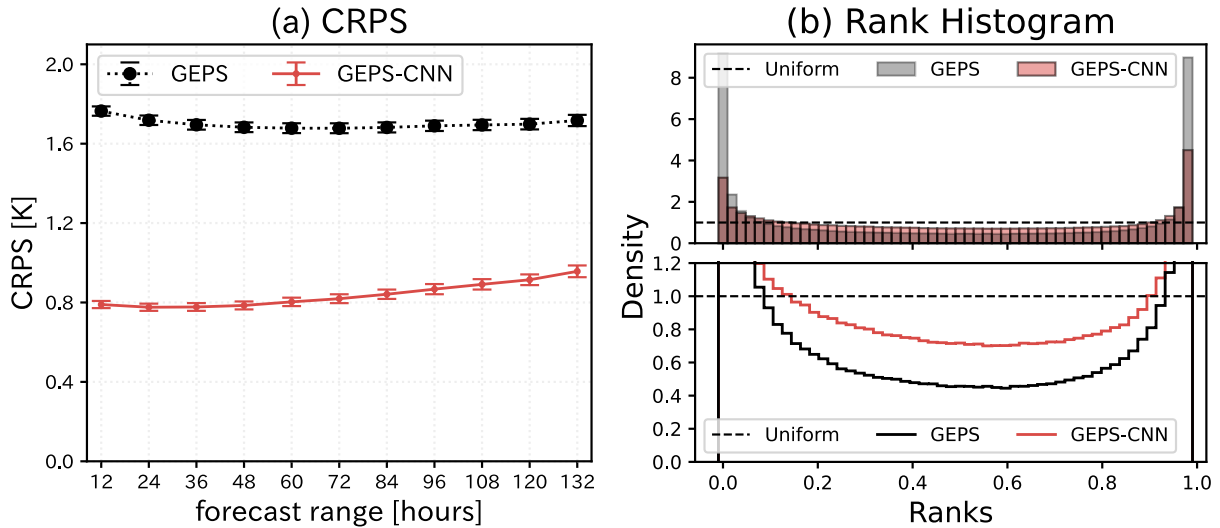


Fig. 7. (a) CRPSs averaged over the experimental period and (b) rank histograms based on all 51 ensemble members of the GEPS and GEPS–CNN at all forecast lead times. The experimental period is from 1 January to 31 December 2022. Error bars represent the 95% confidence intervals.

d. Case Studies

1) FORECAST IMPROVEMENT OVER COMPLEX TERRAIN

Herein, the improvement in temperature forecasts over complex terrain resulting from CNN-based bias correction and super-resolution is validated via case studies. The CF exhibits a low horizontal resolution of 40 km (Fig. 8a), whereas the CF–CNN shows a more accurate temperature distribution (Fig. 8b) that corresponds well with the 5-km topography (Fig. 8c), even over mountainous regions with complex terrain. This indicates that the CNN implicitly learns topographic influences from the NWP fields without using elevation data as an explicit input.

An elevation-corrected baseline forecast (CF–Hcorr) is constructed by adjusting the CF temperature at each grid point using a typical environmental lapse rate of -6 K km^{-1} (e.g., Dodson and Marks 1997) based on the difference between the model orography and analysis elevation. This simple correction reduces the domain-averaged RMSE from 2.1 to 1.6 K but makes the ME more negative from -0.77 to -1.2 K , indicating the presence of negative biases, particularly over the northeastern mountainous regions (Fig. 8d).

In contrast, the CF–CNN (Fig. 8e) substantially reduces these terrain-dependent biases, achieving an ME of -0.23 K and an RMSE of 1.3 K. These results indicate that CNN-based

bias correction and super-resolution enhance the spatial detail and forecast accuracy by effectively incorporating topographic influences. The operational GSM–KF forecast, which runs at a 5-km horizontal resolution with a maximum lead time of 84 h, applies distance- and height-aware interpolation of station observations. Compared with the 20-km GSM forecast (not shown), the GSM–KF forecast shifts the ME from -1.18 to 0.23 K and reduces the RMSE from 2.5 to 1.3 K. However, positive biases that clearly correspond to elevations remain (Fig. 8f). In contrast, the CF–CNN produces smaller errors and exhibits weaker systematic dependence on orography, indicating that it can effectively reduce elevation-related biases. This suggests that the CNN captures continuous topographic influences beyond the discrete grid structure via convolutional and nonlinear corrections using surrounding spatial information.

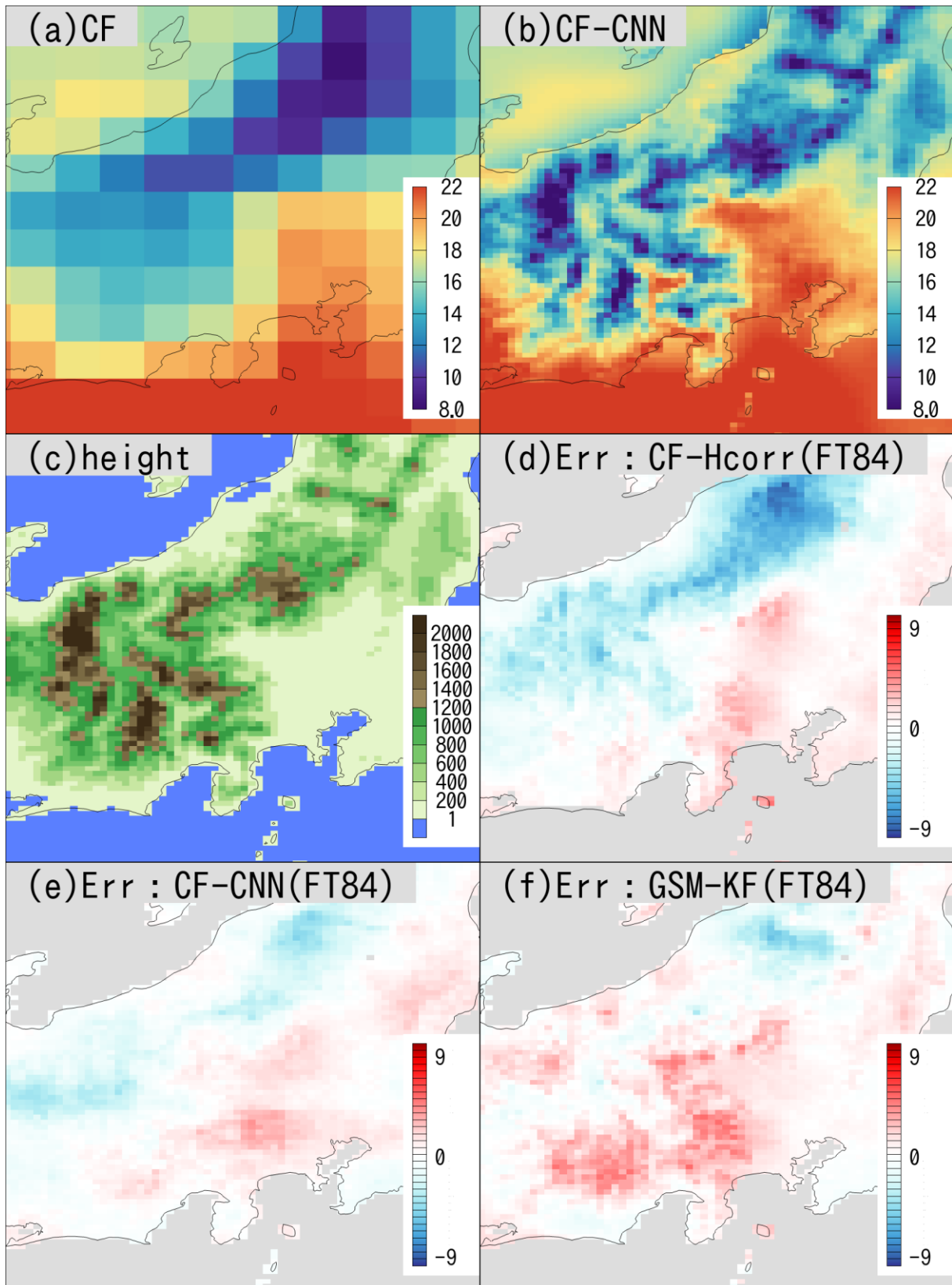


Fig. 8. Surface temperature ($^{\circ}\text{C}$) and forecast error ($^{\circ}\text{C}$) at 1200 UTC (2100 LST) on 13 June 2022. (a) CF, (b) CF-CNN, both initialized at 0000 UTC on 8 June 2022, corresponding to a 132-h lead time. (c) Topography (m). (d) CF error after an elevation correction (CF-

Hcorr), and (e) CF–CNN forecast error, (f) GSM–KF forecast error for the same target time, initialized at 0000 UTC 10 June 2022 with 84-h lead time.

2) NEAR-FREEZING TEMPERATURE FORECAST FOR SNOWFALL PREDICTION

The southern coast of eastern Japan is frequently affected during winter by low-pressure systems that bring heavy snowfall; these are referred to as “South-Coast Cyclones” (Araki 2019). In the Tokyo metropolitan area, such events disrupt transportation and societal activities; however, they are difficult to forecast because they require reliable predictions of both precipitation and near-surface temperature. On the afternoon of 13 February 2022, the Ministry of Land, Infrastructure, Transport and Tourism issued an emergency warning for heavy snowfall (Ministry of Land, Infrastructure, Transport and Tourism 2022). However, the expected transition from rain to snow was delayed by a slower-than-expected nighttime temperature drop, and the heavy snowfall did not occur. Even slight deviations in surface temperature forecasts near the freezing point (0°C) can alter the snow-to-liquid ratio and precipitation type (e.g., snow or rain), leading to substantial differences in snowfall accumulation (Jennings and Molotch 2019; Furuichi and Matsuzawa 2009). As highlighted in this case, temperature forecast errors can lead to substantial overestimations of snowfall events and their associated societal impacts.

The near-surface air temperature threshold separating rain and snow generally ranges from approximately -1 to 2.5°C , depending on regional and environmental factors such as humidity and elevation (Ye et al. 2013; Jennings et al. 2018). Because Japan has a humid midlatitude maritime climate, a relatively warm threshold of 2.5°C is adopted in this case study as the criterion to distinguish snow from rain. Figure 9a shows the GEPS forecast of surface temperature at a 132-h lead time, where the color shading represents the GEPS–EM and the blue, gray, and red contours denote the 2.5°C isotherms for CF, PF, and GEPS–EM, respectively. Both the CF and GEPS–EM, which represent the average of 50 PF members, exhibit a 2.5°C isotherm bisecting the wide plain shown in Fig. 8c, suggesting a potential for snowfall over the lowlands. The GSM forecast with a high horizontal resolution of 20 km (not shown), which employs the same physical parameterization schemes as the CF, shows a similar pattern. However, the CNN-corrected forecasts (CF–CNN and PF–CNN) and their ensemble mean (CNN–EM) show differences. The CF–CNN predicts temperatures below 2.5°C over roughly half of the plain, whereas the CNN–EM predicts temperatures exceeding 2.5°C over almost the entire plain, consistent with the EST (Fig. 9c).

Figures 9d–f show surface temperature errors for the CF–CNN, GSM–KF, and MSM–KF forecasts at the same target time but with 48-h lead times. All forecasts correctly reproduce temperatures above 2.5°C across most of the plain, with relatively small errors. Notably, the CF–CNN does not capture the 2.5°C isotherm position with a 132-h lead time (blue contours in Fig. 9b); however, it successfully reproduces the isotherm at a 48-h lead time (red contours in Fig. 9d), exhibiting comparable performance to those of operational products (GSM–KF and MSM–KF). Furthermore, the CNN–EM correctly predicts the 2.5°C isotherm even with a lead time of 132 h (red contour in Fig. 9b), suggesting that ensemble-based CNN correction yields more stable and reliable forecasts by leveraging probabilistic information from multiple ensemble members.

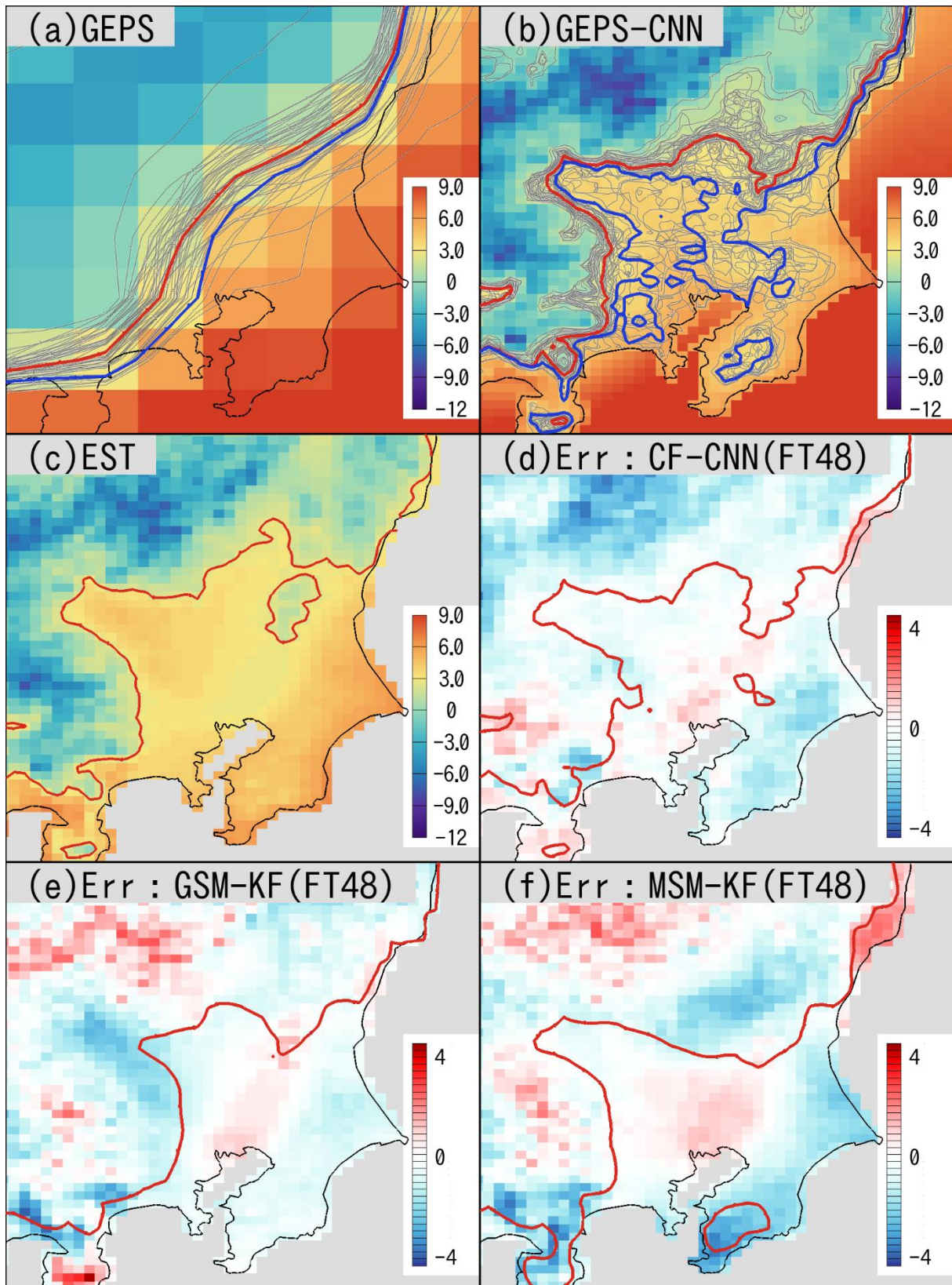


Fig. 9. Colors represent the surface temperatures ($^{\circ}\text{C}$) and forecast error ($^{\circ}\text{C}$) at 1200 UTC (2100 LST) on 13 February 2022 and contours indicate the 2.5°C isotherm. (a) Colors show the GEPS-EM, and the blue, gray, and red contours correspond to CF, PF, and GEPS-

EM, respectively. (b) Colors represent the CNN–EM, and the contours correspond to CF–CNN, PF–CNN, and CNN–EM. All forecasts in (a) and (b) are initialized at 0000 UTC on 8 February 2022 with a 132-h lead time. (c) EST. Forecast for (d) CF–CNN, (e) GSM–KF, and (f) MSM–KF at the same target time with 48-h lead times. Colors denote forecast errors, and red contours indicate the 2.5°C isotherm.

6. Discussion

a. Smoothing or Improving?

We decompose forecast performance into meaningful information (forecast information: FI) and random error (noise error: NE), beyond conventional skill metrics proposed by BG25. Figure 10a shows an FI–NE–ACC diagram similar to that in Fig. 3 of BG25. BG25 plots the Information and Noise metrics defined by FTZP24, the FI and NE defined by BG25 are used herein.

Deterministic forecasts (CF, GSM, and MSM) exhibit a gradual decrease in FI and an increase in NE with increasing forecast lead time while maintaining their activity (distance from the origin). In contrast, the EM forecasts (GEPS–EM and CNN–EM) show decreasing FI, NE, and activity with increasing forecast lead time, eventually approaching the origin. This indicates that the differences in the characteristics of deterministic and EM forecasts (Fig. 10a) are mostly consistent with those reported in BG25. However, the CNN–EM exhibits a higher ACC compared with the CF–CNN, consistent with that in BG25; in contrast, the GEPS–EM maintains an ACC that is nearly identical to that of the CF.

An analysis of the FI and NE shows that the FI increases as the model resolution improves from 40 km for the CF to 20 km for the GSM and 5 km for the MSM. The ordering of NE among the forecasts is consistent with that of the RMSE shown in Fig. 5, indicating that NE appropriately represents the overall magnitude of forecast errors.

Figure 10b presents a comparison of the behaviors of EM (GEPS–EM and CNN–EM), KF-based correction (GSM–KF), and CNN-based post-processing (GSM–CNN, CF–CNN, and PF–CNN); in the figure, the axes are rescaled and the forecast lead time restricted to 72 h. The FI of the GEPS–EM is comparable to the mean FI of the PFs, and both FI and NE are smaller than those of the CF (the same relationship holds among the CNN–EM, PF–CNNs, and CF–CNN). This indicates that the FI and NE are reduced via ensemble averaging. In addition, NE decreases substantially (by an amount larger than the reduction from CF or PFs

to GEPS-EM) when the KF is applied to the GSM, whereas the FI shows no significant difference. In other words, the KF considerably reduces the NE while preserving the FI. In contrast, CNN-based post-processing further suppresses the NE beyond that achieved by the KF (from CF to CF-CNN or from GSM to GSM-CNN) while preserving or even increasing the FI.

In summary, the CNN effectively suppresses forecast errors while preserving the FI. This indicates that CNN-based post-processing reduces forecast errors not via artificial smoothing but via genuine improvements in the forecasts themselves.

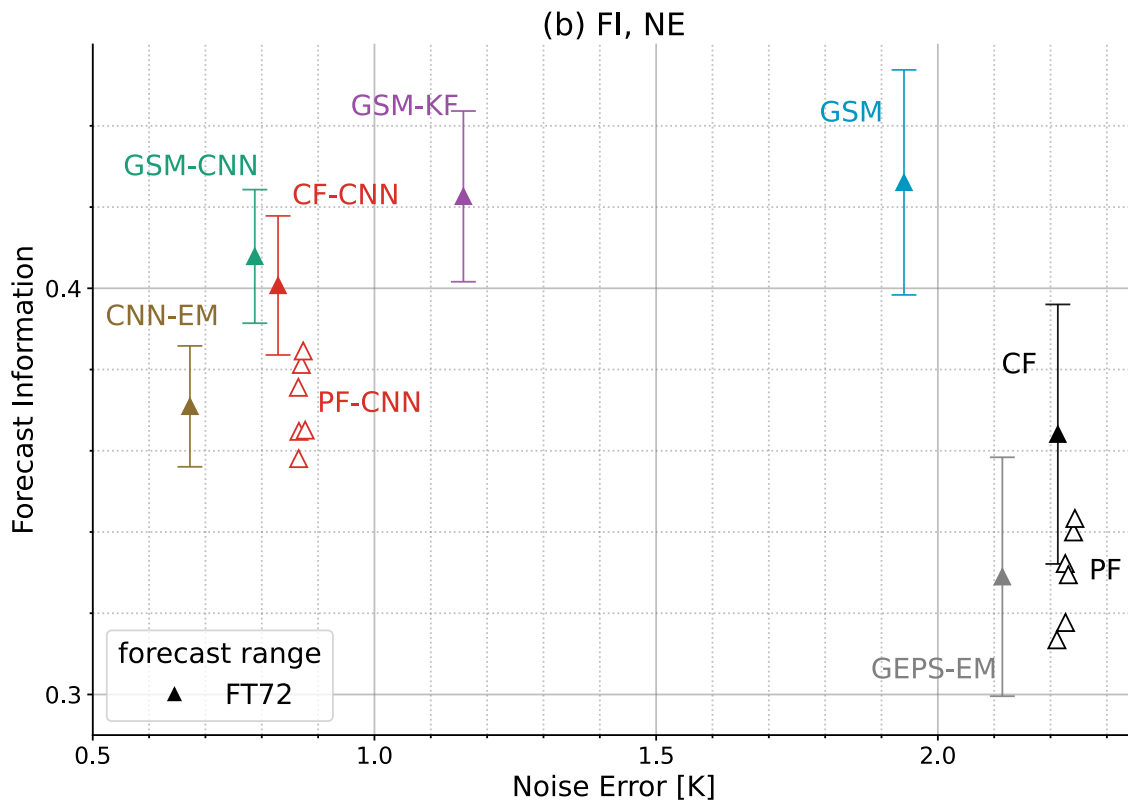
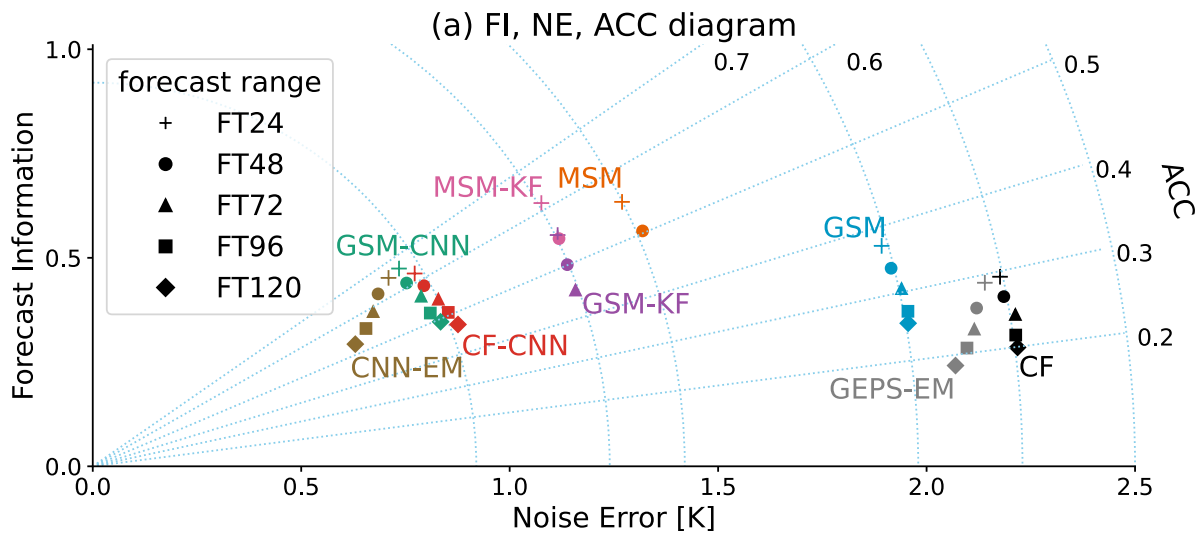


Fig. 10. (a) FI, NE, and ACC diagram and (b) FI–NE plots at representative forecast lead times. The definitions of FI and NE follow those reported by Bonavita and Geer (2025).

b. Limitations: Prediction of Extreme Temperatures

Ensemble averaging inherently smooths forecast data, suppressing extreme temperatures and limiting the ability of the method to predict extreme events such as heatwaves. In the previous section, we demonstrated that the CNN-based post-processing does not suffer from these limitations. However, in this section, we present an example of an extreme heat event for which the CNN-based post-processing still exhibits limitations.

An extraordinary heatwave occurred on 30 June 2022, and the observed surface temperatures exceeded 39°C. Figure 11 compares the surface temperature forecasts for this extreme event, initialized at 0000 UTC on 27 June 2022 and verified at a lead time of 78 h. Panels (a–c) show the GEPS forecast, GEPS–CNN forecast, and EST, respectively. The low-resolution 40-km GEPS forecast (Fig. 11a), shaded for GEPS–EM forecast and contoured for 34°C, fails to capture the extremely high temperatures observed over the plains. The 34°C contour appears only in a few PFs (gray) but not in the GEPS–EM (red). After CNN correction (Fig. 11b), both CNN–EM (red) and the CNN-corrected 36th PF (PF36–CNN; blue) show an extended high-temperature region compared with the original PF36. This indicates that the CNN extrapolates the input information to predict higher temperatures and improves the spatial extent of the warm region; however, the CNN–EM underestimates the maximum intensity.

These forecasts are compared with post-processed deterministic forecasts derived from the 20-km GSM and 5-km MSM. GSM forecasts are downscaled to 5-km resolution using either the KF- or CNN-based post-processing. The 5-km GSM–KF forecast (not shown) more easily represents localized extremes by first applying pointwise bias correction with the KF and then interpolating to the grid. The GSM–CNN (not shown) also shows high-temperature areas more clearly than the GEPS (Fig. 11b), although the predicted temperatures remain lower than the observations. These results indicate that bias correction solely using the KF or CNN cannot fully compensate for the underrepresentation of high temperatures in the GSM input fields. In contrast, the MSM–KF forecast (Fig. 11e), derived from a regional NWP model (MSM) independent of the GSM, reproduces the observed warm-area extent more closely.

For this case, the GEPS–CNN reduces the ensemble spread slightly from 0.93 to 0.84 K (–0.09 K), whereas the CRPS improves substantially from 3.19 to 2.62 K (–0.57 K). This indicates that the improvement in the overall distribution far outweighs the modest reduction in the ensemble spread.

The Q–Q plot of temperature anomalies (Fig. 12) confirms these differences. For the GEPS–EM, the upper tail of the distribution on the warm side lies below the observations (the cross at $p = 0.99$), indicating underestimation of the extreme heat. This feature corresponds to a deficiency in the warm-side upper tail distribution. In contrast, the Q–Q plot for the CNN–EM show that the upper end on the warm side and the overall slope of the curve are closer to the diagonal, indicating improved reproduction of temperature distribution, particularly in the upper-tail distribution. However, the curve remains at a roughly constant distance below the diagonal, indicating that negative biases remain. The MSM–KF, which uses the higher-resolution MSM rather than the GEPS as the input, lies closest to the diagonal in both its overall slope and end points, and it reproduces the observed distribution well over a wide range of quantiles. The failure to fully reproduce the most extreme heat is due to limitations of the CNN itself and the limited information contained in the low-resolution GEPS inputs.

Although CNN correction shows strong potential for enhancing spatial consistency and generalization, the CNN architecture must be further improved and ensemble information must be effectively used for more reliable predictions of pronounced temperature extremes.

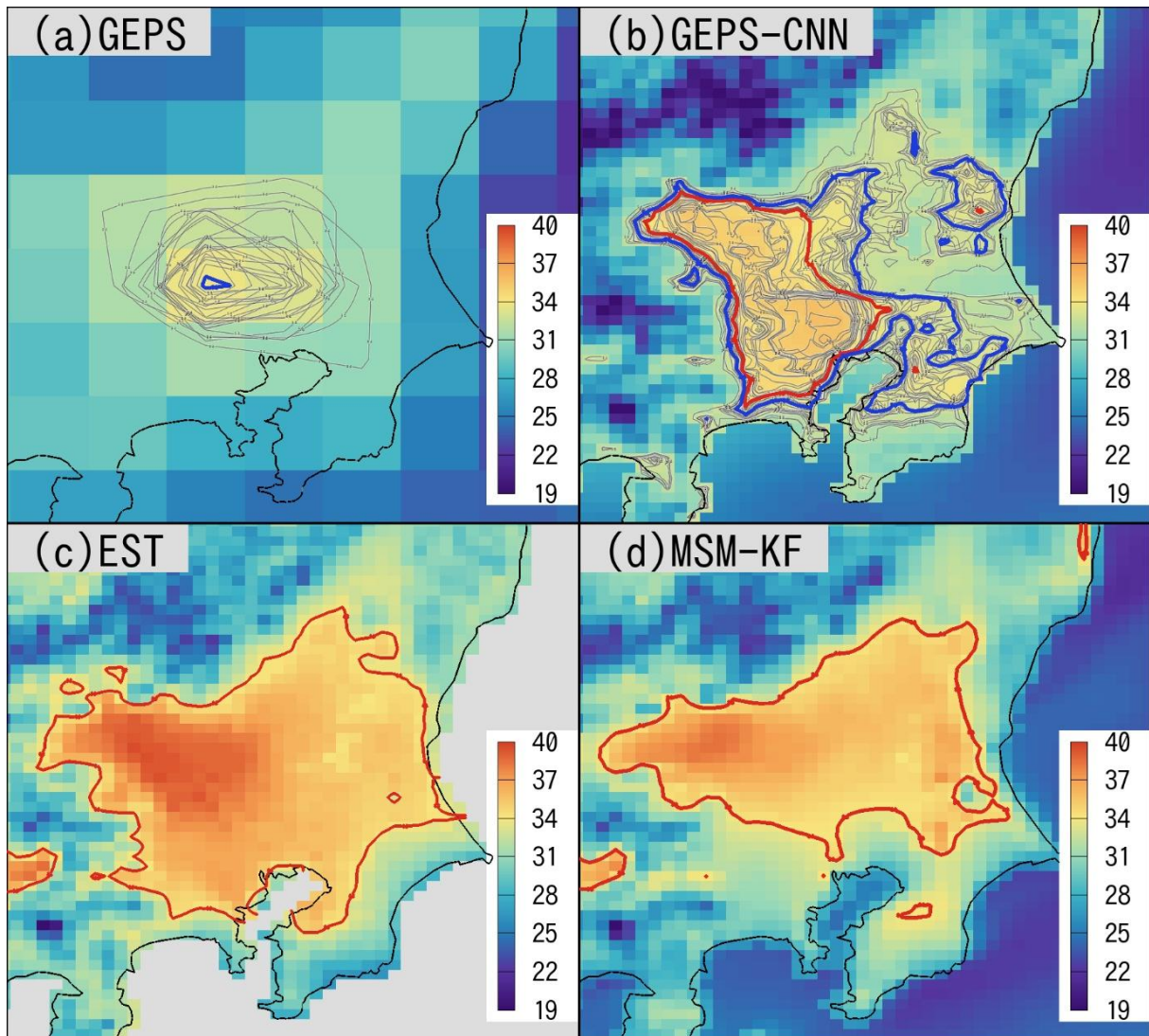


Fig. 11. Surface temperatures ($^{\circ}\text{C}$) for the extreme heat event at 0600 UTC (1500 LST) on 30 June 2022 (forecasts are initialized at 0000 UTC 27 June 2022 with a 78-h lead time). Color shades represent the (a) GEPS-EM, (b) CNN-EM, (c) EST, and (d) MSM-KF. The contours indicate the 34°C isotherm. In (a), gray, red, and blue contours correspond to the PFs, GEPS-EM, and 36th perturbed member (PF36), respectively; in (b) these contours correspond to the PF-CNNs, CNN-EM, and PF36-CNN, respectively.

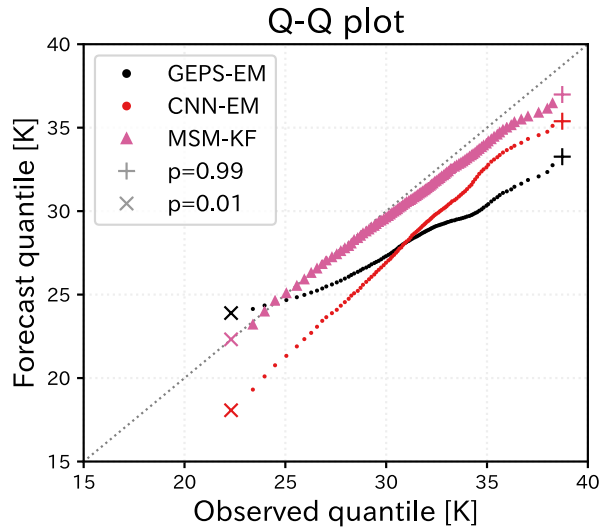


Fig. 12. Q–Q plot of temperatures for the 78-h forecast (initialized at 0000 UTC 27 June 2022). Dots show quantile pairs between observations and forecasts for the GEPS–EM (black) and the CNN–EM (red) and triangles for the MSM–KF (pink). The 1:1 line (gray dotted) indicates perfect agreement. Symbols “+” and “x” indicate the upper ($p = 0.99$) and lower ($p = 0.01$) distribution tails, respectively.

7. Conclusion

To enhance medium-range surface temperature predictions, a post-processing method that integrates CNN-based bias correction and super-resolution with ensemble forecasting is proposed herein. By operating on low-resolution global ensemble model outputs and producing high-resolution forecasts, the CNN overcomes the spatial-resolution limitation of existing ensemble and enables 5-km-class medium-range forecasts under limited computational resources; this is an important advantage for operational systems that rely on low-resolution models to extend their forecast range. Based on the results, the three questions posed in the introduction have been addressed below.

A1. CNN-based post-processing achieved substantial improvements in deterministic and ensemble forecasts. When applied to deterministic forecasts from the JMA global and regional models (GSM and MSM), the CNN substantially reduced the RMSE and ME at all lead times. For the CF, the CF–CNN improved the lead-time-averaged RMSE by 1.2 K (46%) and reduced the corresponding mean error by 0.18 K, outperforming all operational deterministic NWP models and their KF-based methods (GSM–KF and MSM–KF). When combined with ensemble averaging, member-wise CNN correction synergistically reduced both systematic and random forecast errors.

A2. CNNs trained individually using the CF, PF, and GEPS–EM showed similar performances when applied to all ensemble members. These CNNs reduced the lead-time-averaged RMSE of both the CF and PFs, and the resulting ensembles exhibited similar improvements in the SSRs. No statistically significant differences were observed among the three training strategies. These results indicate that training the CNN on a single representative member such as the CF is sufficient. This approach considerably simplifies the design and operational implementation of CNN-based post-processing for ensemble prediction systems.

A3. The CRPS decreased at all lead times, SSR approached 1.0, and the rank histograms became flatter, indicating improved ensemble reliability after CNN-based post-processing. Furthermore, analysis using the FI and NE indicates that unlike simple ensemble averaging, the CNN suppressed the NE while maintaining or even increasing the FI relative to both the ensemble mean and the KF-based post-processing. These forecast improvements resulted from genuine error reduction rather than artificial skill gains via excessive smoothing. This clarifies the relationship between CNN-based post-processing and the smoothing effects of ensemble averaging.

Case studies highlighted the practical benefits of the proposed method. Over complex terrain in central Japan, the CNN produced spatially detailed temperature patterns consistent with 5-km topography and substantially reduced biases that remained after a simple elevation-based correction and even after the GSM–KF. In a near-freezing “South-Coast Cyclone” case, the CNN provided stable and reliable forecasts of the rain–snow transition with a 132-h lead time, comparable to operational products (GSM–KF and MSM–KF) even at shorter lead times. These examples demonstrate that CNN-based bias correction and super-resolution can enhance the spatial detail and temporal consistency in medium-range forecasts wherein small temperature errors have large societal impacts.

Nonetheless, the proposed method has limitations in predicting extreme events. In an extraordinary heatwave case, the CNN expanded the spatial extent of high temperatures and improved the upper-tail distribution compared with the original ensemble mean but still underestimated the maximum intensity. This indicates that the performance of CNN-corrected forecasts in such extremes is fundamentally constrained by the limited predictability of the low-resolution NWP inputs. Although our experiments are limited to Japan, the proposed method is not inherently Japan-specific and can be transferred to other

regions given suitable reference analyses, with retraining or domain adaptation as needed. In future work, incorporating probabilistic forecasting frameworks built on CNN-corrected ensemble outputs can further enhance the reliability of uncertainty quantifications (Rasp and Lerch 2018; Dueben and Bauer 2018; Sønderby et al. 2020). In addition, exploring alternative deep learning architectures such as Vision Transformers, which can better capture the long-range spatial dependencies than CNNs, can improve forecasting in complex or highly nonlinear scenarios (Pathak et al. 2022; Lam et al. 2023).

Acknowledgments.

We sincerely thank Mr. S. Ito and Mr. Y. Shirayama of the Numerical Prediction Development Center at the Japan Meteorological Agency (JMA) and Dr. T. Sekiyama and Dr. D. Hotta of the Meteorological Research Institute (MRI) at JMA for their valuable discussions. This work was supported by the Japanese Society for the Promotion of Sciences (JSPS) KAKENHI (Grant Number 24H00278, 25H00784, 25K01483) and by a Fugaku General Access Project (Project ID: hp250210).

Data Availability Statement.

The source code of the CNN models used in this study is available upon request, subject to collaborative research agreement with the MRI. Numerical weather-prediction model output datasets of the JMA are operationally provided via the Japan Meteorological Business Support Center (JMBSC; <http://www.jmbsc.or.jp/en/index-e.html>). Datasets not available through JMBSC may be obtained through collaborative research agreement with the MRI and/or the JMA.

REFERENCES

- Anadranistakis, M., K. Lagouvardos, V. Kotroni, and H. Eleftheriadis, 2004: Correcting temperature and humidity forecasts using Kalman filtering: Potential for agricultural protection in Northern Greece. *Atmos. Res.*, **71**, 115–125, <https://doi.org/10.1016/j.atmosres.2004.03.007>.
- Araki, K., 2019: Study on heavy snowfall associated with ‘South-Coast Cyclones’: Present state and future work. *Meteor. Res. Notes*, **241**, 605–614. (*in Japanese*).

- Bauer, P., A. Thorpe, and G. Brunet, 2015: The quiet revolution of numerical weather prediction. *Nature*, **525**, 47–55, <https://doi.org/10.1038/nature14956>.
- Buizza, R., and T. N. Palmer, 1995: The singular-vector structure of the atmospheric global circulation. *J. Atmos. Sci.*, **52**, 1434–1456, [https://doi.org/10.1175/1520-0469\(1995\)052<1434:TSVSOT>2.0.CO;2](https://doi.org/10.1175/1520-0469(1995)052<1434:TSVSOT>2.0.CO;2).
- Chen, S., X. Fang, and M. Khayatnezhad, 2024: Forecasting for electricity demand utilizing enhanced Inception-V4 using improved Osprey optimization. *Sci. Rep.*, **14**, 30832, <https://doi.org/10.1038/s41598-024-81487-8>.
- Cho, D., C. Yoo, B. Son, J. Im, D. Yoon, and D.-H. Cha, 2022: A novel ensemble learning for post-processing of NWP Model's next-day maximum air temperature forecast in summer using deep learning and statistical approaches. *Wea. Climate Extreme*, **35**, 100410, <https://doi.org/10.1016/j.wace.2022.100410>.
- Dueben, P. D., and P. Bauer, 2018: Challenges and design choices for global weather and climate models based on machine learning. *Geosci. Model Dev.*, **11**, 3999–4009, <https://doi.org/10.5194/gmd-11-3999-2018>.
- Dodson, R., and D. Marks, 1997: Daily air temperature interpolated at high spatial resolution over a large mountainous region. *Climate Res.*, **8**, 1–20, <https://doi.org/10.3354/cr008001>.
- Dosovitskiy, A., and Coauthors, 2021: An image is worth 16x16 words: Transformers for image recognition at scale. *Proc. 9th Int. Conf. on Learning Representations (ICLR 2021)*, Virtual Only, Computational and Biological Learning Society, Paper 3458, <https://doi.org/10.48550/ARXIV.2010.11929>.
- Frisvold, G. B., and A. Murugesan, 2013: Use of Weather information for agricultural decision making. *Wea. Climate Soc.*, **5**, 55–69, <https://doi.org/10.1175/WCAS-D-12-00022.1>.
- Furuichi, Y., and N. Matsuzawa, 2009: Snowfall amount guidance. Textbook for Numerical Weather Prediction, No. 42, Japan Meteorological Agency, Tokyo, Japan, 27–38, <https://www.jma.go.jp/jma/kishou/books/nwptext/42/chapter2.pdf>. (in Japanese).
- Glahn, H. R., and D. A. Lowry, 1972: The use of model output statistics (MOS) in objective weather forecasting. *J. Appl. Meteor. Climatol.*, **11**, 1203–1211, [https://doi.org/10.1175/1520-0450\(1972\)011<1203:TUOMOS>2.0.CO;2](https://doi.org/10.1175/1520-0450(1972)011<1203:TUOMOS>2.0.CO;2).

- Hersbach, H., 2000: Decomposition of the continuous ranked probability score for ensemble prediction systems. *Wea. Forecasting*, **15**, 559-570, [https://doi.org/10.1175/1520-0434\(2000\)015<0559:DOTCRP>2.0.CO;2](https://doi.org/10.1175/1520-0434(2000)015<0559:DOTCRP>2.0.CO;2).
- Hess, P., and N. Boers, 2022: Deep learning for improving numerical weather prediction of heavy rainfall. *J. Adv. Model. Earth Syst.*, **14**, e2021MS002765, <https://doi.org/10.1029/2021MS002765>.
- Homleid, M., 1995: Diurnal corrections of short-term surface temperature forecasts using the Kalman filter. *Wea. Forecasting*, **10**, 689–707, [https://doi.org/10.1175/1520-0434\(1995\)010<0689:DCOSTS>2.0.CO;2](https://doi.org/10.1175/1520-0434(1995)010<0689:DCOSTS>2.0.CO;2).
- Hunt, B. R., E. J. Kostelich, and I. Szunyogh, 2007: Efficient data assimilation for spatiotemporal chaos: A local ensemble transform Kalman filter. *Phys. D*, **230**, 112–126, <https://doi.org/10.1016/j.physd.2006.11.008>.
- Ikuta, Y., T. Fujita, Y. Ota, and Y. Honda, 2021: Variational data assimilation system for operational regional models at Japan Meteorological Agency. *J. Meteor. Soc. Japan*, **99**, 1563–1592, <https://doi.org/10.2151/jmsj.2021-076>.
- Inoue, T., T. T. Sekiyama, and A. Kudo, 2024: Development of a temperature prediction method combining deep neural networks and a Kalman filter. *J. Meteor. Soc. Japan*, **102**, 415–427, <https://doi.org/10.2151/jmsj.2024-020>.
- Japan Meteorological Agency, 2016: Launch of provision of estimated weather distribution products. Tech. rep., 422, Japan Meteorological Agency, Tokyo, Japan, 16 pp, <https://www.data.jma.go.jp/add/suishin/jyouhou/pdf/422.pdf>. (in Japanese).
- Japan Meteorological Agency, 2023: Numerical weather prediction models. Outline of the Operational Numerical Weather Prediction at the Japan Meteorological Agency, Japan Meteorological Agency, Tokyo, Japan, 53–156, https://www.jma.go.jp/jma/jma-eng/jma-center/nwp/outline2023-nwp/pdf/outline2023_03.pdf.
- Jennings, K. S., and N. P. Molotch, 2019: The sensitivity of modeled snow accumulation and melt to precipitation phase methods across a climatic gradient. *Hydrol. Earth Syst. Sci.*, **23**, 3765–3786, <https://doi.org/10.5194/hess-23-3765-2019>.

- Jennings, K. S., T. S. Winchell, B. Livneh, and N. P. Molotch, 2018: Spatial variation of the rain–snow temperature threshold across the Northern Hemisphere. *Nat. Commun.*, **9**, 1148, <https://doi.org/10.1038/s41467-018-03629-7>.
- Kawabata, T., H. Seko, K. Saito, T. Kuroda, K. Tamiya, T. Tsuyuki, Y. Honda, and Y. Wakazuki, 2007: An assimilation and forecasting experiment of the nerima heavy rainfall with a cloud-resolving nonhydrostatic 4-dimensional variational data assimilation system. *J. Meteor. Soc. Japan*, **85**, 255–276, <https://doi.org/10.2151/jmsj.85.255>.
- Kawabata, T., T. Kuroda, H. Seko, and K. Saito, 2011: A cloud-resolving 4DVAR assimilation experiment for a local heavy rainfall event in the Tokyo metropolitan area. *Mon. Wea. Rev.*, **139**, 1911–1931, <https://doi.org/10.1175/2011MWR3428.1>.
- Krizhevsky, A., I. Sutskever, and G. E. Hinton, 2012: ImageNet classification with deep convolutional neural networks. *Adv. Neural Inf. Process. Syst. 25 (NeurIPS 2012)*, Lake Tahoe, NV, Neural Inf. Process. Syst. Foundation, 1097–1105, https://papers.nips.cc/paper_files/paper/2012/hash/c399862d3b9d6b76c8436e924a68c45b-Abstract.html.
- Kudo, A., 2022: Statistical post-processing for gridded temperature prediction using encoder–decoder-based deep convolutional neural networks. *J. Meteor. Soc. Japan*, **100**, 219–232, <https://doi.org/10.2151/jmsj.2022-011>.
- Kuroki, Y., 2017: Improvement of gridded temperature guidance and changes of guidance for snowfall amount and categorized weather. Textbook for Numerical Weather Prediction, No. 50, Japan Meteorological Agency, Tokyo, Japan, 94–101, <https://www.jma.go.jp/jma/kishou/books/nwptext/50/chapter4.pdf>. (in Japanese).
- Lam, R., A. Sanchez-Gonzalez, M. Willson, P. Wirnsberger, M. Fortunato, F. Alet, S. Ravuri, T. Ewalds, Z. Eaton-Rosen, W. Hu, A. Merose, S. Hoyer, G. Holland, O. Vinyals, J. Stott, A. Pritzel, S. Mohamed, and P. Battaglia, 2023: Learning skillful medium-range global weather forecasting. *Science*, **382**, 1416–1421, <https://doi.org/10.1126/science.adi2336>.
- Leith, C. E., 1974: Theoretical skill of Monte Carlo forecasts. *Mon. Wea. Rev.*, **102**, 409–418, [https://doi.org/10.1175/1520-0493\(1974\)102<0409:TSOMCF>2.0.CO;2](https://doi.org/10.1175/1520-0493(1974)102<0409:TSOMCF>2.0.CO;2).
- Lorenz, E. N., 1969: The predictability of a flow which possesses many scales of motion. *Tellus*, **21**, 289–307, <https://doi.org/10.1111/j.2153-3490.1969.tb00444.x>.

- Ministry of Land, Infrastructure, Transport and Tourism, 2022: Emergency statement concerning heavy snowfall. Tech. doc., Ministry of Land, Infrastructure, Transport and Tourism, Tokyo, Japan, 3 pp, <https://www.mlit.go.jp/common/001463621.pdf>. (*in Japanese*).
- Palmer, T. N., 2001: A nonlinear dynamical perspective on model error: A proposal for non-local stochastic-dynamic parametrization in weather and climate prediction models. *Quart. J. Roy. Meteor. Soc.*, **127**, 279–304, <https://doi.org/10.1002/qj.49712757202>.
- Pathak, J., S. Subramanian, P. Harrington, S. Raja, A. Chattopadhyay, M. Mardani, T. Kurth, D. Hall, Z. Li, K. Azizzadenesheli, P. Hassanzadeh, K. Kashinath, and A. Anandkumar, 2022: FourCastNet: A global data-driven high-resolution weather model using adaptive Fourier neural operators. arXiv preprint, <https://doi.org/10.48550/arXiv.2202.11214>.
- Rasp, S., and S. Lerch, 2018: Neural networks for postprocessing ensemble weather forecasts. *Mon. Wea. Rev.*, **146**, 3885–3900, <https://doi.org/10.1175/MWR-D-18-0187.1>.
- Sannohe, Y., 2018: Temperature guidance. Report of Numerical Prediction Division, No. 64, Japan Meteorological Agency, Tokyo, Japan, 132–143, <https://www.jma.go.jp/jma/kishou/books/nwpreport/64/chapter4.pdf>. (*in Japanese*).
- Sayeed, A., Y. Choi, J. Jung, Y. Lops, E. Eslami, and A. K. Salman, 2023: A Deep convolutional neural network model for improving WRF simulations. *IEEE Trans. Neural Netw. Learn. Syst.*, **34**, 750–760, <https://doi.org/10.1109/TNNLS.2021.3100902>.
- Sha, Y., D. J. Gagne II, G. West, and R. Stull, 2022: A hybrid analog-ensemble, convolutional-neural-network method for post-processing precipitation forecasts. *Mon. Wea. Rev.*, **150**, 1495–1515, <https://doi.org/10.1175/MWR-D-21-0154.1>.
- Simonyan, K., and A. Zisserman, 2015: Very deep convolutional networks for large-scale image recognition. *Proc. 3rd Int. Conf. on Learning Representations (ICLR 2015)*, Computational and Biological Learning Society, San Diego, CA, Paper 1409.1556, <https://doi.org/10.48550/arXiv.1409.1556>.
- Skamarock, W. C., 2004: Evaluating mesoscale NWP models using kinetic energy spectra. *Mon. Wea. Rev.*, **132**, 3019–3032, <https://doi.org/10.1175/MWR2830.1>.

- Sønderby, C. K., L. Espeholt, J. Heek, M. Dehghani, A. Oliver, T. Salimans, S. Agrawal, J. Hickey, and N. Kalchbrenner, 2020: MetNet: A neural weather model for precipitation forecasting. arXiv preprint, <https://doi.org/10.48550/arXiv.2003.12140>.
- Stensrud, D. J., 2007: *Parameterization Schemes: Keys to Understanding Numerical Weather Prediction Models*. Cambridge University Press, 273 pp.
- Swinbank, R., and Coauthors, 2016: The TIGGE project and its achievements. *Bull. Amer. Meteor. Soc.*, **97**, 49–67, <https://doi.org/10.1175/BAMS-D-13-00191.1>.
- Toth, Z., and E. Kalnay, 1997: Ensemble forecasting at NCEP and the breeding method. *Mon. Wea. Rev.*, **125**, 3297–3319, [https://doi.org/10.1175/1520-0493\(1997\)125<3297:EFANAT>2.0.CO;2](https://doi.org/10.1175/1520-0493(1997)125<3297:EFANAT>2.0.CO;2).
- Wakayama, I., T. Imai, T. Kitamura, and K. Kobayashi, 2020: About estimated weather distribution. *Wea. Serv. Bull.*, **87**, 1–18, <https://www.jma.go.jp/jma/kishou/books/sokkou/87/vol87p001.pdf>.
- Wang, J., J. Chen, J. Du, Y. Zhang, Y. Xia, and G. Deng, 2018: Sensitivity of ensemble forecast verification to model bias. *Mon. Wea. Rev.*, **146**, 781–796, <https://doi.org/10.1175/MWR-D-17-0223.1>.
- Wang, L., L. Xin, Y. Zhu, Y. Fang, and L. Zhu, 2023: Associations between temperature variations and tourist arrivals: Analysis based on Baidu Index of hot-spring tourism in 44 cities in China. *Environ. Sci. Pollut. Res.*, **30**, 43641–43653, <https://doi.org/10.1007/s11356-023-25404-y>.
- Wilks, D. S., 2011: *Statistical Methods in the Atmospheric Sciences*. Academic Press 704 pp.
- World Meteorological Organization, 2023: *Manual on the Global Data-Processing and Forecasting System* (WMO-No. 485). 20, Geneva, Switzerland, ISBN 978-92-63-10485-4, <https://library.wmo.int/idurl/4/35703>.
- World Meteorological Organization, 2024: *Guide to Meteorological Instruments and Methods of Observation* (WMO-No. 8). 43, Geneva, Switzerland, ISBN 978-92-63-100085, <https://doi.org/10.59327/WMO/CIMO/1>.
- Wu, P.-Y., T. Kawabata, and L. Duc, 2025: The importance of perturbation rank in ensemble simulations. *Mon. Wea. Rev.*, **153**, 247–261, <https://doi.org/10.1175/MWR-D-24-0067.1>.

- Xia, Y., J. N. Van Ommeren, P. Rietveld, and W. Verhagen, 2013: Railway infrastructure disturbances and train operator performance: The role of weather. *Transp. Res. Part D: Transp. Environ.*, **18**, 97–102, <https://doi.org/10.1016/j.trd.2012.09.008>.
- Ye, H., Cohen J., and Rawlins M., 2013: Discrimination of solid from liquid precipitation over northern Eurasia using surface atmospheric conditions. *J. Hydrometeor.*, **14**, 1345–1355, <https://doi.org/10.1175/JHM-D-12-0164.1>.
- Yin, B., Y. Chen, and X. Xu, 2024: How does temperature change affect residents' health? A multidimensional health perspective. *Wea. Climate Soc.*, **16**, 771–784, <https://doi.org/10.1175/WCAS-D-24-0041.1>.